Rock typing of diagenetically induced heterogeneities – A case study from a deeply-buried clastic Rotliegend reservoir of the Northern German Basin

Alexander C. Monsees[a,*], Benjamin Busch[a], Nadine Schöner[b], Christoph Hilgers[a]

[a] Department Structural Geology and Tectonics, Institute of Applied Geosciences, Karlsruhe Institute of Technology (KIT), Adenauerring 20a, 76131, Karlsruhe, Germany
[b] Wintershall Dea GmbH, Labor Wietze, Industriestraße 2, 29323, Wietze, Germany

Keywords:
Reservoir quality evolution
Diagenesis
Matrix permeability
Sandstone
Rotliegend
Northern German Basin

A B S T R A C T

Reservoir quality of sandstones is mainly derived from their permeability and porosity. As a result, porosity-reducing processes need to be understood in order to evaluate and model reservoir quality in sandstones. This case study from a Rotliegend gas reservoir in the Northern German Basin utilizes petrophysical measurements in conjunction with petrography in order to assess reservoir qualities and define rock types. The most significant diagenetic factors influencing the development of the IGV (intergranular volume) are quartz cementation due to low illite grain coating coverages on grain to IGV interfaces and chemical compaction due to pronounced illite grain coating coverages on grain to grain interfaces. Where large proportions of the interface between adjacent grains are coated by illite, stronger chemical compaction (pressure dissolution) was observed to occur. This chemical compaction reduces the IGV, and thus open pore space.

Permeabilities measured under decreasing confining pressures from 50 to 2 MPa were used to determine the pressure sensitivities of permeability (David et al., 1994), which ranged from 0.005 to 0.22 MPa^{-1}. The pressure sensitivity of permeability, porosity and permeability were linked to the petrographic texture, implying three different major rock types: Type A is characterized by an uncemented petrographic texture with high porosities (avg.: 9.8%), high permeabilities (avg.: 126 mD), and low pressure sensitivities of permeability (avg.: 0.019 MPa^{-1}). Type B is intensely cemented with reduced porosities (avg.: 4.0%), reduced permeabilities (avg.: 0.59 mD), and increased pressure sensitivities of permeability (avg.: 0.073 MPa^{-1}). Type C is characterized by intense chemical compaction leading to the lowest porosities (avg.: 1.8%) and permeabilities (avg.: 0.037 mD) in concert with the highest pressure sensitivity of permeability (avg.: 0.12 MPa^{-1}). The heterogeneity induced by diagenesis will have an impact on recoverable resources and flow rates in both hydrocarbon and geothermal projects in similar siliciclastic reservoirs.

Credit author statement

Alexander C. Monsees: Methodology, Software, Formal analysis, Investigation, Writing Original Draft, Writing Review & Editing, Visualization, Benjamin Busch: Conceptualization, Methodology, Writing Original Draft, Writing Review & Editing, Supervision, Project administration, Nadine Schöner: Validation, Resources, Christoph Hilgers: Supervision, Funding acquisition.

1. Introduction

Clastic reservoir rocks are of significant economic interest as host rocks for natural gas or oil in the hydrocarbon industry, as interim storage medium for natural gas and biogas, as potential long term storage medium for CO_2 sequestration, and as potential aquifers in geothermal projects (Selley, 1998; Bachu, 2000; Legarth et al., 2005; Ambrose et al., 2008; Morad et al., 2010). Diagenetic processes, for instance authigenic cementation, as well as chemical and mechanical compaction, have a major impact on the quality of clastic reservoirs (Paxton et al., 2002; Taylor et al., 2010; Becker et al., 2017; Busch et al., 2017; Wüstefeld et al., 2017a; Worden et al., 2018). For example, early diagenetic processes, such as grain coatings, may inhibit quartz cementation (Heald and Larese, 1974; Esch et al., 2008; Ajdukiewicz et al., 2010; Taylor et al., 2010; Ajdukiewicz and Larese, 2012; Busch et al., 2018, 2020). Further diagenetic alteration of the sandstones additionally modifies the available pore space by mineral precipitation and dissolution (Worden and Burkley, 2003; Worden et al., 2018), impacting reservoir quality development (Gaupp et al., 1993; Gaupp

* Corresponding author.
E-mail address: alexander.monsees@kit.edu (A.C. Monsees).

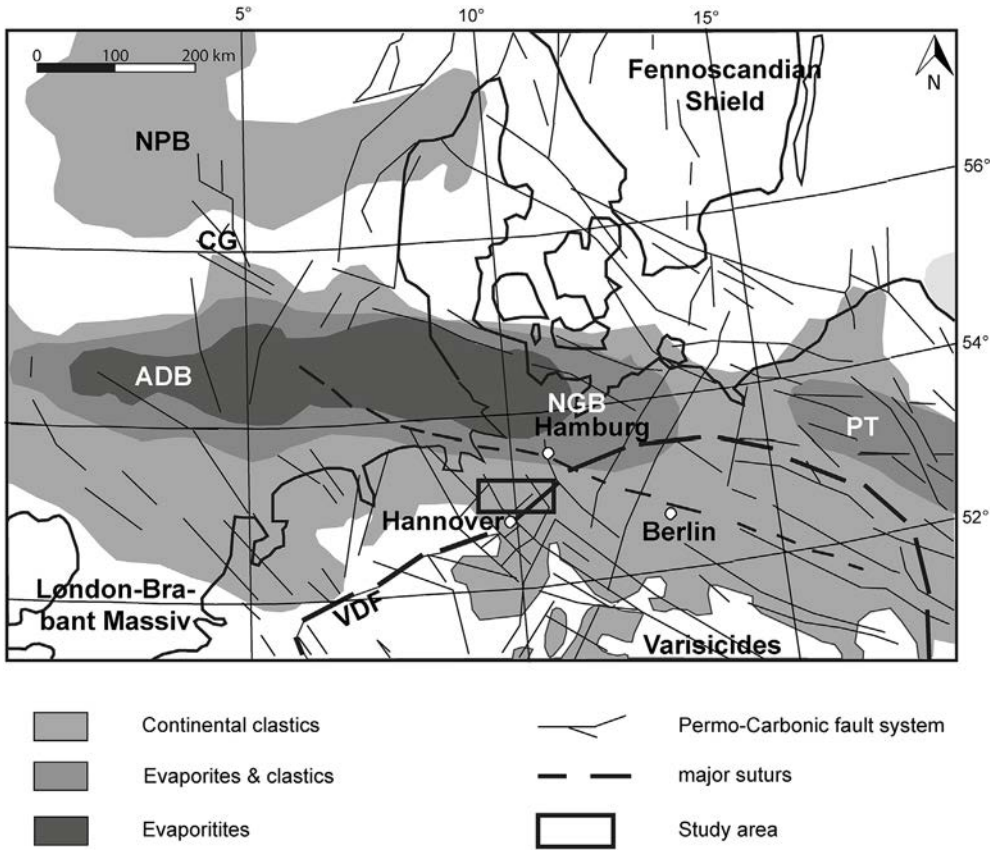

Fig. 1. Schematic map illustrating the extent of the siliciclastic Rotliegend during the time of deposition in Central Europe. Modified from Moeck et al. (2009), based on Ziegler (1990), Ziegler and Dezes (2005) and Gast and Gundlach (2006). NPB: Northern Permian Basin, CG: Central Graben, ADB: Anglo-Dutch Basin, NGB: North German Basin, PT, Polish Trough, VDF: Variscan Deformation Front.

and Jos, 2011; Bahlis and De Ros, 2013; Taylor et al., 2015; Desbois et al., 2016; Becker et al., 2017; Becker et al., 2019; Busch et al., 2019; Busch et al., 2020). Compaction induced modifications of the detrital grain framework are also affected by diagenetic alterations, as e.g. ce ments can preserve the intergranular volume (IGV) (Paxton et al., 2002; Line et al., 2018). Micro scale sedimentary and structural features may have a profound impact on permeability (Gaupp et al., 1993; Morad et al., 2010; Taylor et al., 2010, 2015; Busch et al., 2015, 2018; Schmidt et al., 2018), e.g. in eolian dunes, which are characterized by sand bodies with tabular cross bedding, separated by bounding surfaces (Chandler et al., 1989). As a result, detailed micro scale studies are necessary in order to understand and assess porous reservoir rock quality, and might prove to be a useful tool during exploration and production of associated industries.

The eolian Rotliegend sandstones are important reservoirs for nat ural gas in Central Europe (Gast et al., 2010). This study investigates Rotliegend sandstone samples of the Havel subgroup from two wells in Northern Germany. The extent of Rotliegend deposits during the time of deposition and the most important structural features are shown in Fig. 1.

The aim of this study is to characterize and quantify the impact of diagenetic processes on reservoir properties by linking petrographic with petrophysical information. Based on the combination of petro physical measurements with petrographic information, rock types with regards to their reservoir quality will be established. The rock typing does not only consider petrophysical values e.g. porosity, but also the process behind the reservoir quality reduction or preservation during burial and diagenesis.

2. Geological setting

The study area is located on the Pompeckj Block (PB) in a North South orientated graben, part of the fan shaped graben system (Plein and van Adrichem Boogaert, 1995; Gast and Gundlach, 2006) between Hamburg, Hannover and Bremen (Fig. 1) that limits the extent of the studied reservoir with faults on its eastern and western margin. The North German Basin is an element of the Southern Permian Basin (SPB), which also incorporated the Anglo Dutch Basin and the Polish Trough (Fig. 1) (Ziegler, 1990; Gast et al., 2010). The extent of the Northern German Basin is limited by the Variscides in the south, the Anglo Dutch Basin to the west, the Fennoscandian Shield to the North and the Polish Trough to the East (Fig. 1). The SPB was formed between the front of the Variscan orogenic belt and the Mid North Sea High (Katzung, 1988; Ziegler, 1990). West north west to west trending faults were initiated by the Variscan collision between Gondwana and Laurussia (Ziegler, 1990). From Stephanian (Upper Carboniferous) onwards, the precursor of the SPB was subsided after a phase of under plating, crustal thinning and uplift (Geluk, 2005; Gast and Gundlach, 2006; Gast et al., 2010). During the Carboniferous, the area of the SPB was drifting northwards from the equator, residing in the desert belt between 10° and 30° on the northern hemisphere during the Permian (Scotese and Langford, 1995; Blakey and Wong, 2003; Glennie, 2007). The base of the Permian is characterized by the Base Permian Unconformity (Ziegler, 1990), which locally leads to a hiatus of up to 60 Ma between Upper Carboniferous and Upper Rotliegend deposits (Geluk, 1999). E W extension during the Permian induced the formation of N to NNW striking faults (Lohr et al., 2007). The Lower Rotliegend can be found in the subsurface and at outcrops in Northern Germany and primarily comprises of rhyolites, andesites and smaller amounts of basalts (Hoth et al., 1993; Gast and Gundlach, 2006; Schöner, 2006; Gast et al., 2010). The Upper Rotlie gend in Germany is divided into Upper Rotliegend I which is restricted to rift basins and grabens, and Upper Rotliegend II, whose deposits can be traced throughout the whole SPB (Schröder et al., 1995) (Fig. 2). The Havel and Elbe subgroups of the Upper Rotliegend II (Fig. 2) are sub divided into two formations each and have a total sediment thickness of 2500 m (Plein and van Adrichem Boogaert, 1995), which was deposited

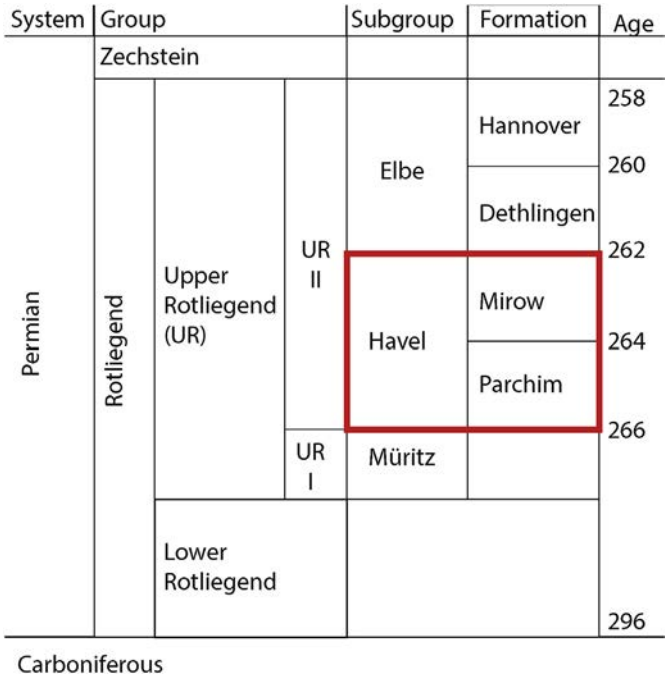

Fig. 2. Stratigraphic subdivision of the German Rotliegend using ages from Menning (1995), modified from Schöner (2006). The studied sandstones belong to the Havel subgroup (red box). (For interpretation of the references to color in this figure legend, the reader is referred to the Web version of this article.)

over a time span of 5 10 Ma in total (Menning, 1995). Depositional environments in the Upper Rotliegend were influenced by an arid to semi arid climate and included playas, ergs and saline lakes (Gaupp et al., 1993; Kiersnowski et al., 1995; Gast et al., 2010; Fryberger et al., 2011; Kiersnowski, 2013). A large saline playa lake was located in the basin center (Fig. 1) (Gast et al., 2010). The sedimentary systems de veloped from alluvial fans close to the Variscan orogen into sandflats and dunes in distal areas (Gast et al., 2010; Fryberger et al., 2011). Playa sediments were deposited around the lake at the center of the basin (Fig. 1) (Fryberger et al., 2011). Sediments for the ergs were supplied from the Variscan orogen at the southern margin of the North German Basin (Kiersnowski et al., 1995; McCann, 1998; Rieke, 2001). Deposition was controlled by cyclic climatic forcing controlling the lake level and the subsequent shift of facies whereas the frequencies of the cycles correspond to the Milankovitch cycles of precession (20 ka), short eccentricity (100 ka) and long eccentricity (400 ka) (Gast, 1993; Sweet, 1999), which may also be identified in purely eolian environ ments (Kocurek et al., 2001). Each of the four main formations of the Upper Rotliegend II (Fig. 2) shows 7 major cycles (Gast, 1993; Sweet, 1999). Throughout the Upper Rotliegend II, a general trend towards higher lake levels in the SPB can be observed from the purely fluvio eolian Havel Subgroup towards increasingly lacustrine conditions at the top of the Elbe Subgroup (Legler and Jörg, 2008). The depositional setting of the studied area (Fig. 1) is an erg and shows dunes and dry sandflats as depositional facies. Rotliegend siliciclastic deposition was terminated by the ingression of the Zechstein sea and the resulting precipitation of evaporites and carbonates during the Upper Permian (Smith, 1979; Glennie and Buller, 1983). Rotliegend sandstones were buried rapidly up to 3000 m depth until the end of the Triassic (Schwarzer and Littke, 2007). The German Triassic is divided into the fluvio lacustrine sedimentation of the Buntsandstein, followed by the marine Muschelkalk ingression, which was succeeded by continental brackish to hypersaline deposits of the Keuper (Bachmann et al., 2010). From Keuper to Jurassic, the Northern German Basin experienced an extensional phase in NNE SSW direction leading to W to NW striking faults (Lohr et al., 2007). The onset of the Jurassic led to the flooding of the epicontinental basin in the area of the SPB by the Tethys Ocean to the south and the Boreal Ocean to the north (Lott et al., 2010). Towards the end of the Jurassic, the study area was uplifted by over 1000 m (Schwarzer and Littke, 2007), forming the Pompeckj Block. The in version caused the erosion of the majority of Jurassic strata (Binot et al., 1993). Marine epicontinental sedimentation of carbonates and marls, as well as subsequent burial recommenced in the study area during the Late Aptian transgression, which was induced by a eustatic sea level rise in concert with increased subsidence rates (Ziegler, 1990; Vejbæk et al., 2010). The kinematic regime shifted from E W compression along the existing NW striking fault system from Santonian to Campanian to N S compression from the Coniacian to Maastrichtian (Lohr et al., 2007), which can be linked to the mechanical coupling of Europe and Africa over Iberia (Kley and Voigt, 2008). Throughout the Tertiary, primarily sands and clays were deposited (Knox et al., 2010). The structural de velopment of the Cenozoic is governed by normal faulting induced by salt diapirism along reactivated fault zones (Lohr et al., 2007) and ac celerated subsidence of the Northern German Basin due to collisional processes and subsequent lithosphere folding and faulting associated with the formation of the Pyrenees and the Alps (Lohr et al., 2007; Kley and Voigt, 2008).

3. Materials & methods

A total of 55 polished thin sections orientated across the bedding plane originating from two Northern German gas wells approximately 2 km apart, were studied. The thin sections were impregnated with a blue dyed epoxy resin, prepared to a thickness of 30 μm and stained with Alizarin Red S. Twenty thin sections from well A representing a total vertical depth (TVD) range of 4698 4720 m (sampling interval approximately 1 m) and 35 thin sections from well B, representing a TVD range of 4674 4706 m (sampling interval approximately 1 m) were studied. The studied samples belong to the Havel subgroup of the Upper Rotliegend.

All 55 thin sections were point counted (300 counts) on a grid ad justed to the maximum grain size (determined by image analysis) with a semi automated Pelcon Point Counter installed on a Leitz Aristomet microscope.

The sandstone compositions were classified according to Folk (1980). The intergranular volume (IGV) was classified after Paxton et al. (2002). Compactional and cementational porosity loss as well as compactional indices were calculated after Lundegard (1992). The percentage of clay mineral coatings on grain to IGV (GTI) interfaces was assessed on at least 50 grains per sample (Busch et al., 2017). The length of the grain's illite coating in contact with the IGV was measured and divided by the length of the total grain circumference in contact with the IGV. Comparator images for different clay mineral coverages are shown in Fig. 3. Percentages of illite coatings on grain to grain (GTG) interfaces were evaluated analogously. All microscope images were taken with a Jenoptik Progres Gryphax camera, mounted on a Leica DMLP microscope.

Cathodoluminescence was studied with an optical cath odoluminescence system by Cambridge Image Technology Ltd (CITL) mounted on a Leitz Dialux microscope. The system was operated with a voltage of 15 ± 1 kV for carbonate cements and accessories and 20 ± 1 kV for quartz. Applied currents ranged from 325 to 350 μA.

Petrophysical measurements were conducted on cylindrical 30 mm plugs. For all samples used in petrophysical analyses a thin section is available. Decane porosity (ϕ, n = 49) was measured using the Archimedes or flotation/liquid resaturation method with decane as flotation medium. The rock samples were dried at 120 °C, weighed and put in a desiccator. The desiccator was evacuated and afterwards the samples were saturated with decane. Samples were then put in a pressure chamber filled with decane at 90 bar for one day. Decane saturated samples were weighed in decane and outside decane under normal air pressure. The relative decane porosity was calculated from

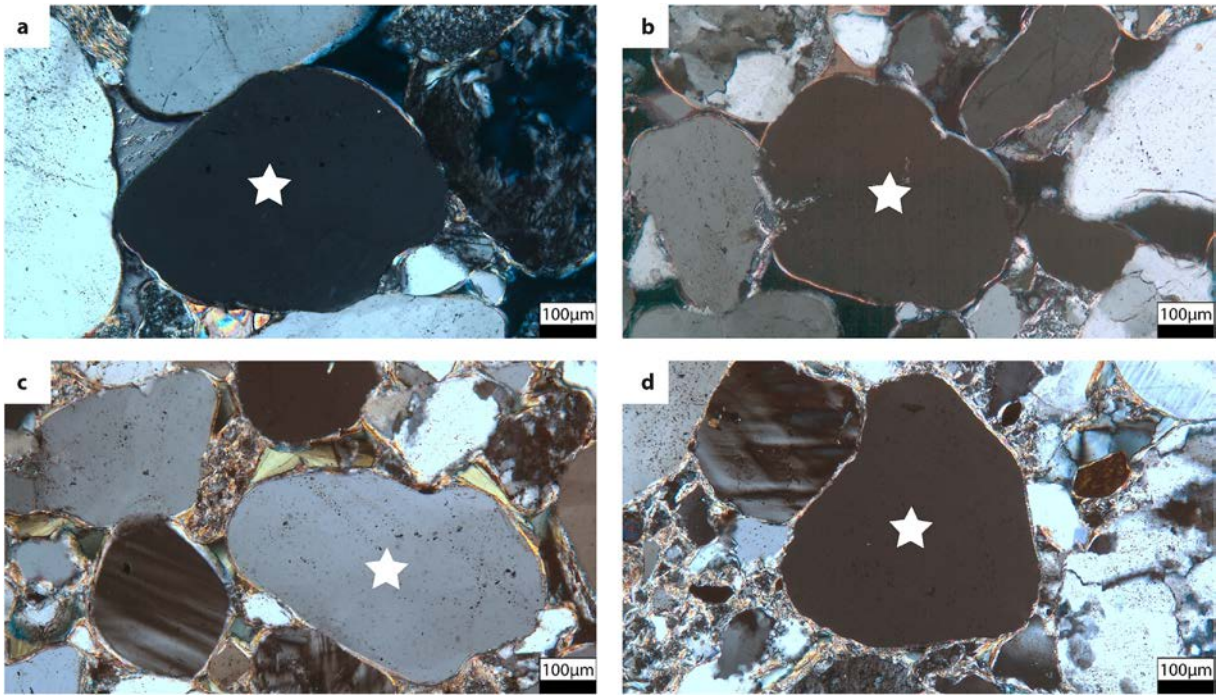

Fig. 3. Clay-coating coverages on grain to grain (GTG) contacts were quantified by visual image analysis. The grains used for these examples are indicated by a white star. a) Almost no clay coatings on GTG contacts (coverage 10%, sample A 12). b) Around 30% illite on GTG contacts (sample B 04). c) 60% coverage GTG interfaces (sample B 10). d) Complete illite coverages at GTG contacts (> 95%, sample B 15).

the determined differences in weight (Kuila et al., 2014). The statistical error of the arithmetic mean was determined by dividing the standard deviation by the square root of the number of samples.

Klinkenberg corrected permeability (κ, n = 49) was measured at a constant confining pressure of 1.2 MPa on 49 plugs with an air permeameter manufactured by Westphal Mechanik using oil free lab air (80% N_2, 20% O_2) as the permeant. Permeabilities were also measured under decreasing confining pressures (50, 30, 10, 5, 2 MPa) at room temperature (22 ± 1 °C) on n = 46 samples using helium as a permeant ($\eta = 1.97 * 10^{-5} Pa * s$ at 22 °C). All samples were loaded up to 50 MPa confining pressure. Permeabilities were measured during the unloading cycle in a DBHS 50 150 pressure cell from GL Test Systems GmbH. The cell is fitted with a hydraulic pump to adjust confining pressures. Apparent permeabilities were measured at varying p_{mean} and corrected for slip flow (Amann Hildenbrand et al., 2015), using the Klinkenberg correction (Klinkenberg, 1941).

The pressure sensitivity coefficients of permeability (γ) were calculated after David et al. (1994).

4. Results

4.1. Petrography

4.1.1. Detrital composition

Subarkoses (well A: 50%, well B: 68%) and lithic arkoses (well A: 50%, well B: 23%) are the most abundant sandstone types (Fig. 4). Sublitharenites (well B: 3%), feldspathic litharenites (well B: 3%) and arkoses (well B: 3%) were not present in samples from well A (Fig. 4). The main constituent of the samples is detrital quartz, including mono and polycrystalline, as well as undulose quartz and metaquartzite varieties (well A: 52 73%, mean 60%; well B: 44 71%, mean 62%) (Fig. 5 a, c, d, supplementary material). Feldspars (well: A 9 18%, mean 13%; well B: 8 21%, mean 13%) (Fig. 5 a, b, d, supplementary material) and rock fragments (well A: 3 16%, mean 8%; well B: 2 15%, mean 7%) are common (Fig. 5 d, supplementary material). Detrital matrix was encountered with a mean of < 1%, although its distribution

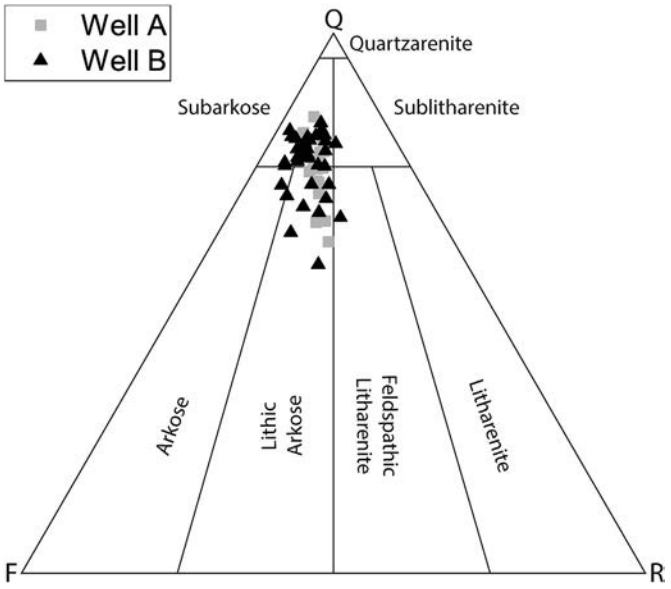

Fig. 4. Sandstone classification after Folk (1980) based on point-counting results. The studied samples are dominantly subarkoses and lithic arkoses and show no distinct differences between the studied wells.

varies (well A: 0 4%; well B: 0 10%) (Fig. 5 c). Mica and accessories such as zircon, rutile, tourmaline or amphibole are very rare (mean < 1%). Chert is very rarely present (mean < 1%).

Most of the detrital quartz is monocrystalline (Fig. 5 c, d), although every sample contains a varying amount of polycrystalline grains and quartzite as well. The feldspars are dominated by K feldspars (mean 8%) showing microcline textures and parquet twinning (Fig. 5d). Plagioclase grains (mean < 0.3%) show lamellar twinning. Rock fragments (mean 4%) consist of volcanic rock fragments, plutonic rock fragments, metamorphic rock fragments, and sedimentary fragments. Volcanic rock fragments (mean 3%) are of silicic or feldspathic origin

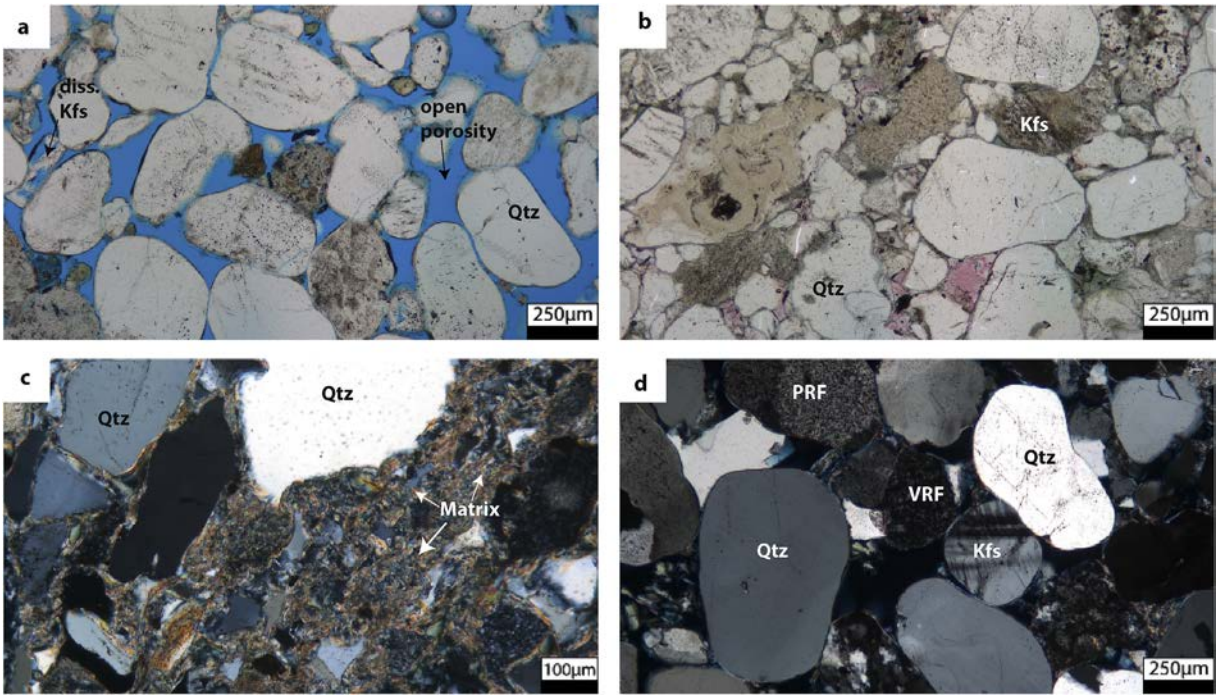

Fig. 5. Photomicrographs of detrital components in thin-sections under plane-polarized light (ppl) and crossed-polarized light (xpl). a) Porous subarkose of well A, representative for the sections with porosities above 10% (ppl, sample A 04). b) This lithic arkose is characterized by its very low porosities (ppl, sample B 20). c) Detrital clay matrix, which is abundant in some samples of the lower section of well B (xpl, sample B 16). d) Lithic arkose showing the most common detrital components (xpl, sample A 08). Qtz = quartz, Kfs = potassium feldspar, PRF = plutonic rock fragment, VRF = volcanic rock fragment.

(Fig. 5 d) and show porphyritic, unidirectional textures. Plutonic rock fragments (mean 1%) (Fig. 5 d) are characterized by large, idiomorphic crystals of predominately feldspathic or felsic composition (supplementary material). Sedimentary rock fragments (shale, siltstone and sandstone) contribute around 1% of the overall composition, while low grade metamorphic rock fragments like schists and phyllites occur very rarely (mean < 1%) (supplementary material). The dominating grain size is coarse skewed medium sand, which shows well to moderately well sorting (supplementary material).

4.1.2. Authigenic phases

The most abundant authigenic pore filling phases are syntaxial quartz cement (well A: 1 9%, mean 4%; well B: 1 15%, mean 3%) (Fig. 6 a) and calcite cement (well A: 0 7%, mean 2%, pore filling; well B: 0 8%, mean 1%) (Fig. 6 b), which has a poikilotopic texture (Fig. 6 e). Quartz cements often occur as euhedral overgrowths (Fig. 6 a). Calcite cements appear in two distinct textures. The poikilotopic texture appears to stabilize the grain framework and prevent contacts between detrital grains (Fig. 6 e). The other texture engulfs euhedral syntaxial quartz cements and pore filling chlorite (Fig. 6 g, h). Barite cements (Fig. 6 c) and anhydride cements (Fig. 6 d) may contribute up to 5% in individual samples, but their mean occurrence is below 1%. Anhydrite occupies open pores, engulfing pore lining illite clay minerals (Fig. 7 d) without showing interactions with other pore filling blocky cements. Barite was encountered only in well A. Barite cements were observed to engulf euhedral quartz cements (Fig. 7 e, f). Halite cement, feldspar cement, and gypsum occur in traces in individual samples.

Illite cements (well A: 2 7%, mean 4%; well B: 1 13%, mean 4%) occur in every sample as a pore lining phase (Fig. 6 d) on detrital grains and in some samples as a very rare (< 1%) pore filling phase (Fig. 6 f) as well. The pore lining illite phase shows a tangential texture, encompassing detrital grains with an illite coating (Fig. 6 d). Chlorite cements (well A: 0 5%, mean 2%, pore filling; well B: 0 7%, mean 1%) (Fig. 6 b) occur only as a pore filling phase. Two different forms of pore filling chlorite can be distinguished: vermicular chlorite (Fig. 6 b) occurs in pores that are uncemented besides the vermicular chlorite, and completely pore occluding occurrences (Fig. 5 c) were observed in heavily compacted samples. Replacements of feldspars by illite and volcanic rock fragments by chlorite were consistently observed to be very rare (well A: 0 1%, mean < 1%; well: B 0 1%, mean < 1%).

Cathodoluminescence analyses aided the identification of authigenic quartz cements in samples containing prominent dissolution seams, where irregular grain shapes and the absence of grain coating material impact the optical assessment (Fig. 7). Feldspars showed light blue luminescence, while detrital quartz showed mostly night blue and purple luminescence (Fig. 7 b). Authigenic quartz was identified by structural relationships (Fig. 7 a), and showed no luminescence (Fig. 7 b). Samples with well developed dissolution seams contain below 3.3% quartz cement, which is supported by cathodoluminescence images showing mainly luminescing detrital quartz grains (Fig. 7 c, d). Non luminescent barite was observed to engulf non luminescent euhedral authigenic quartz (Fig. 7 e, f). Pore filling calcite luminesces bright orange (Fig. 7 e, f).

4.1.3. IGV, optical porosity, compaction and texture

The IGV shows comparable ranges in both wells (well A 12 24%, mean: 17%; well B 11 26%, mean 17%). Authigenic minerals are the main contributor to the IGV (well A: 9 19%, mean 13%; well B: 7 21%, mean 14%) (Fig. 8 a). Intergranular optical porosity (stained in blue, compare Fig. 5 a) primarily occurs along the bedding plane of less cemented beds, and ranges from < 1 to 9% (mean: 4%) in well A and from 0 to 11% (mean: 1%) in well B based on point counting. Intragranular optical porosity in feldspars and cherts does not contribute to the IGV and is of minor importance for the total optical porosity (well A: mean 1%; well B: mean < 1%).

The porosity loss in both wells was primarily induced by mechanical compaction based on the assessment of compactional indices (Fig. 8 b) after Lundegard (1992). Compactional indices range from 0.63 to 0.88 (well A avg.: 0.79, well B avg.: 0.76, supplementary material). A relationship between more continuous illite coatings on GTG interfaces

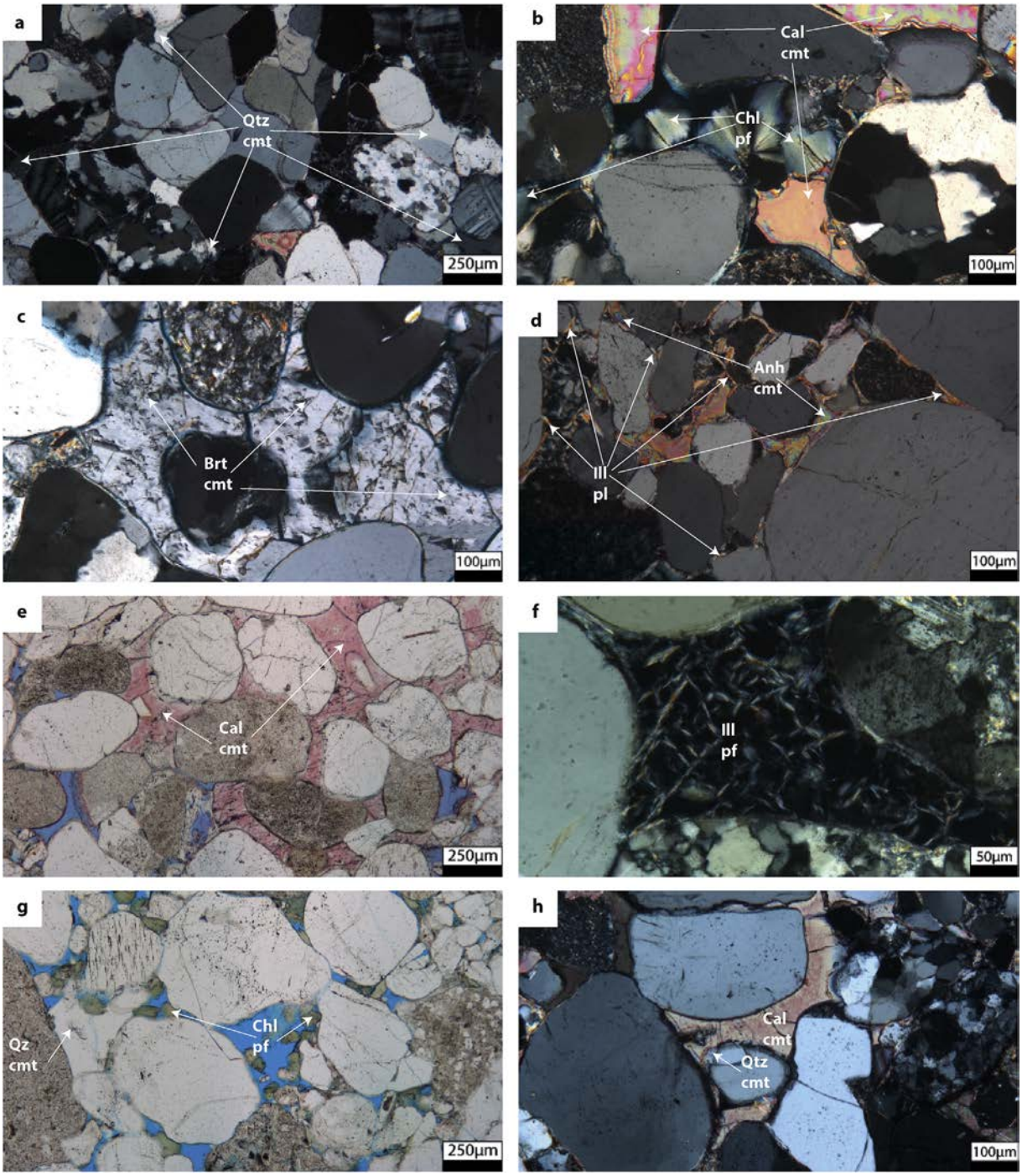

Fig. 6. Photomicrographs of authigenic components in thin-sections under crossed-polarized light (xpl) and plane polarized light (ppl). a) Quartz grains overgrown by authigenic quartz due to low clay mineral coverages (here: 40.7%) on GTI interfaces (xpl, sample B 28). b) Calcite cement occupies open pores, and is limited by pore-filling vermicular chlorite (xpl, sample A 02). c) Barite cement occupying pore-space (xpl, sample A 03). d) Smaller patches of pore-occluding anhydride cement, and illite along the detrital grains (xpl, sample B 23). e) Poikilotopic calcite patches occurred as dominant pore-filling phase (locally up to 10%) in some horizons (ppl, sample B 09). f) Mesh-work illite was observed on pore throats and in open pores with an overall occurrence of < 1% (xpl, sample B 08). g) Authigenic quartz was observed to overgrow pore-filling vermicular chlorite (ppl, sample A 05). h) Interactions between quartz cement and calcite cement were rarely observed. Small rims of authigenic quartz on their detrital grains were observed to be overgrown by calcite (xpl, sample B 01). GTI: grain to IGV interface, Qtz cmt: authigenic quartz, Chl pf: pore-occluding chlorite, Ill pl: grain-coating tangential illite, Ill pf: pore-filling meshwork illite, Cal cmt: calcite cement, Brt cmt: Barite cement, Anh cmt: Anhydrite cement.

and the IGV was observed (Fig. 8 c). More continuous illite coatings (> 40% coverage) on GTG interfaces occurred in samples with lowest IGVs (< 15%) (Fig. 8 c). Generally, the more surface at GTG contacts is covered by illite, the lower the IGV. Quartz cements primarily occur where pore lining clay minerals were not continuously covering quartz grains (Fig. 6 a). Mostly continuous illite coatings on grain to IGV (GTI) interfaces negatively correlate with the amount of authigenic quartz cements (Fig. 8 d). Samples with grain coating coverages above 75% show little to no authigenic quartz (< 3%) (Fig. 8 d).

Three main petrographic types were identified based on their

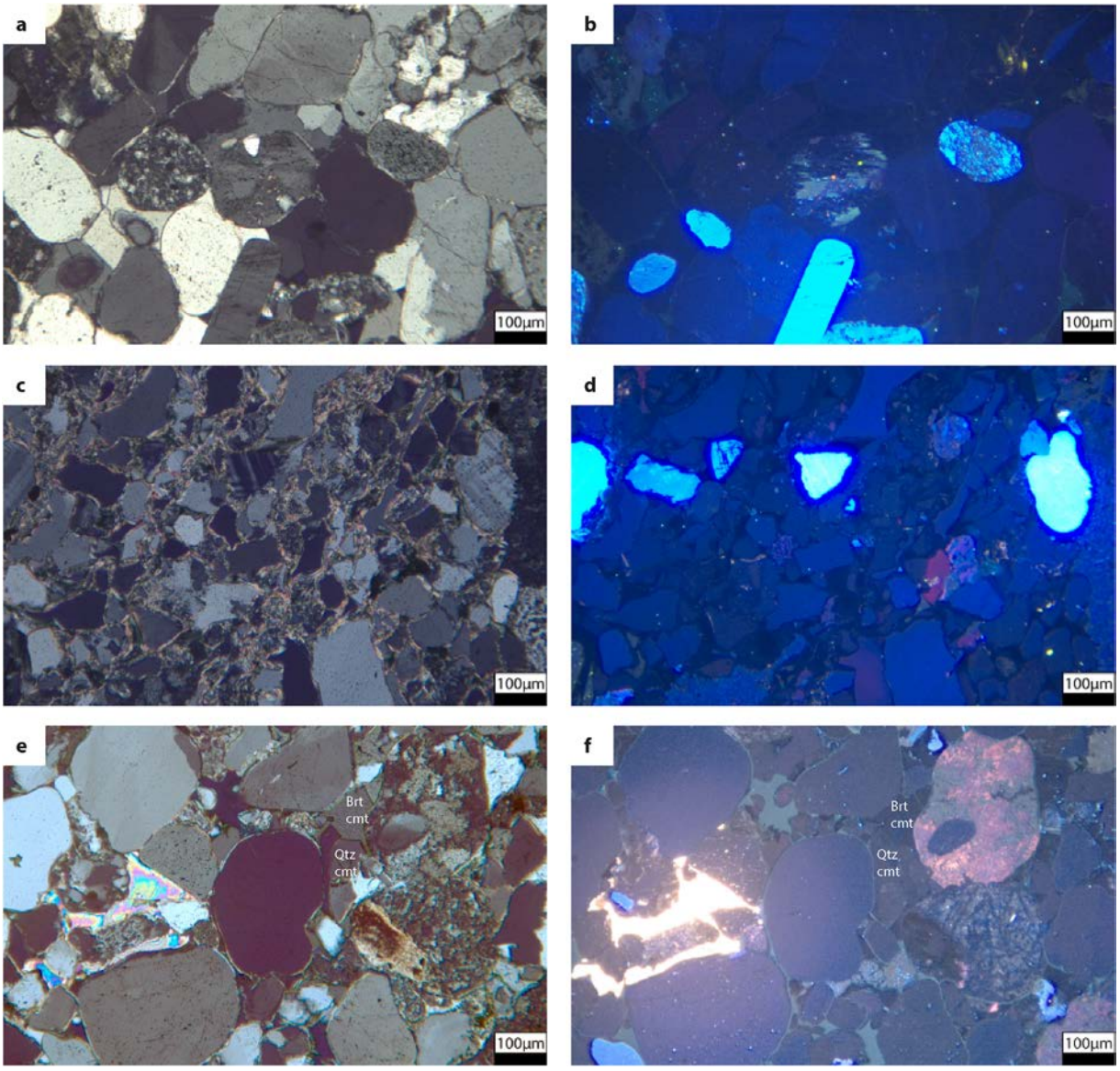

Fig. 7. Photomicrographs of authigenic and detrital quartz under crossed-polarized light (a, c & e) and cathodoluminescence (b, d & f). a & b) Detrital quartz is characterized by purple and night blue luminescence, while authigenic quartz does not show any luminescence at all. c & d) Photomicrographs of dissolution seam. Cathodoluminescence reveals that the quartz in this chemical compaction seam is detrital, while illite (bright color in xpl and chlorite appear non-luminescent. K-Feldspar shows bright blue luminescence. e & f) Euhedral authigenic quartz being enclosed by barite cement, while plagioclases show purple luminescence. Calcite shows bright orange luminescence. (For interpretation of the references to color in this figure legend, the reader is referred to the Web version of this article.)

texture and clay mineral coverage by petrographic observation, and based on assemblages of blocky pore filling cements (quartz, carbo nates, anhydride, barite, halite, feldspar, and gypsum) by point counting.

Type A showed open intergranular porosity along the bedding planes (Fig. 5 a) with small to intermediate amounts of blocky pore filling cements (avg.: 8.6%). The sorting along the bedding planes is very good, however there are pronounced differences in grain sizes between different beds. Consequently, porosities are also bound to the bedding, showing generally higher porosities in beds with coarser grain sizes. Clay minerals occur mainly on GTI interfaces (avg. GTI coverage: 74.0%), while clay minerals on GTG interfaces are less common (avg. GTG coverage: 20.6%).

Type B is characterized by only locally visible open porosity due to intense cementation (Fig. 5 b) by blocky pore filling cements (avg.: 10.2%). The IGVs are comparable to type A, as well as the good sorting along the bedding planes. There are less GTI coatings (avg. GTI cov erage: 62.1%) than in type A, however the amount of GTG coatings is increased (avg. GTG coverage: 27.3%) in comparison.

Type C samples (Fig. 5 c) show no optical porosity and abundant dissolution seams, visible by serrated contacts between detrital quartz rich grains. Coarse grained beds in type C are primarily composed of rock fragments. Type C shows high clay mineral coverages on both GTI interfaces (avg. GTI coverage: 75.8%) and GTG interfaces (avg. GTG coverage: 45.7%) in concert with less abundant blocky pore filling ce ments (avg.: 7.5%).

4.2. Petrophysical measurements

Decane porosity ranges from 0.6% to 14.5% (Fig. 9 a, Table 1, supplementary material), with an arithmetic mean of 6.0 ± 0.5%. Air permeability (1.2 MPa confining pressure) ranges from 0.009 mD to 781 mD (mean 0.96 mD) (Fig. 9 a, supplementary material). The highest permeabilities were observed in medium to well sorted sand stones with distinct bedding features.

With decreasing confining pressures from 50 to 2 MPa, He

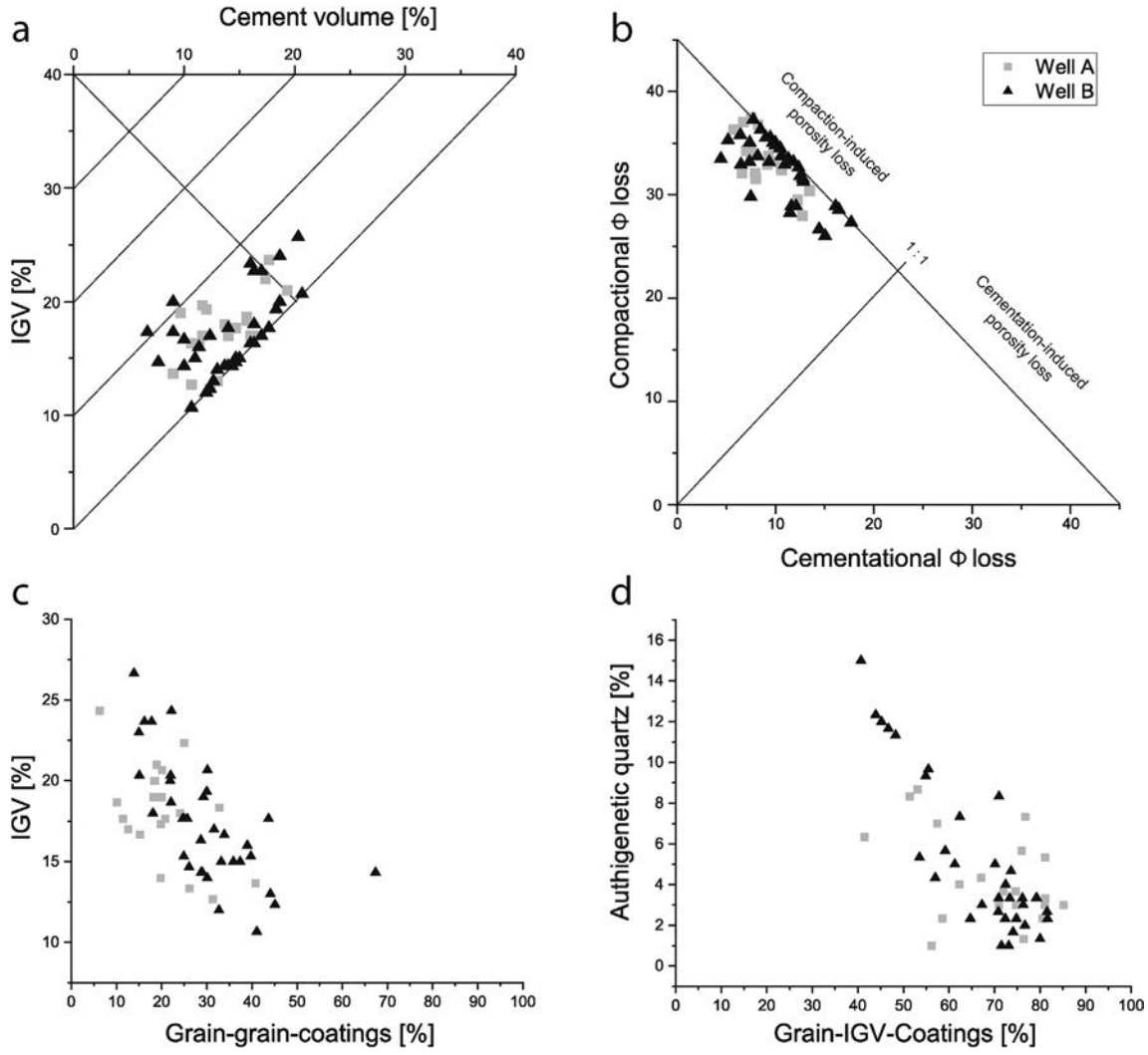

Fig. 8. a) Houseknecht diagram (Houseknecht, 1987) illustrating the relationship between inter-granular volume (IGV) and cement volume in wells A and B. b) Scatter plot of compactional vs cementational porosity loss (Lundegard, 1992) illustrating the dominance of porosity loss by compaction compared to porosity loss by cementation in both well A and well B. c) Scatter plot of the IGV compared to the coverage of illite coatings on grain to grain interfaces (GTG), showing lower IGVs in case of more continous GTG coatings. d) Scatter plot of quartz cementation compared to the illite grain-coat coverage of grains in contact with the IGV, showing the inhibiting effect that grain coatings can have on syntaxial quartz cements.

permeabilities are increased (Fig. 9 b). At 50 MPa confining pressure, permeabilities range from 0.00002 to 176 mD, whereas at 2 MPa confining pressure, permeabilities range from 0.008 to 287 MPa. Cal culated γ coefficients range from 0.005 to 0.222 MPa^{-1} (supplementary material), and show higher γ values (> 0.06 MPa^{-1}) in less porous ($< 6\%$ decane porosity) (Fig. 9 c) and in less permeable samples (< 1 mD) (Fig. 9 d). Smaller γ values (< 0.06 MPa^{-1}) are calculated for samples with higher porosity ($> 6\%$ decane porosity) and higher per meability (> 1 mD).

5. Discussion

5.1. Paragenetic sequence

5.1.1. Early diagenesis

Cementation, dissolution, replacements, and mechanical and che mical compaction were interpreted relative to each other (Fig. 10). Mechanical compaction started due to increasing vertical stresses during burial and reduced porosities throughout early diagenesis, until the maximum of mechanical compaction was reached (Paxton et al., 2002). The burial history relating the subsidence and tectonic devel opment with diagenetic alteration is based on basin modeling conducted by Schwarzer and Littke (2007).

Considering the paleo environment of arid dune to sand flat de posits (e.g. Schöner (2006)), evaporation likely enabled the formation of anhydride (Fig. 6 d) and very local halite during early diagenesis. The occurrence of anhydride in large pores suggests its formation to pre or syndate extensive mechanical compaction (Fig. 6 d). Due to the presence of rather continuous tangential illite grain coatings on both GTI and especially at GTG interfaces in the samples, syn depositional formation of clay mineral grain coatings is inferred (Schöner, 2006; Molenaar and Felder, 2018). Pore lining smectite precursors are inter preted to have been present and recrystallized during burial diagenesis (Gaupp et al., 1993; Liewig and Clauer, 2000; Storvoll et al., 2002; Ajdukiewicz et al., 2010; Molenaar and Felder, 2018). These smectite precursors likely formed from dust input of the arid environment, leading to clay infiltration during or shortly after deposition and pos sible pedogenesis (Molenaar and Felder, 2018). The early formation of these grain coatings is additionally supported by the paragenesis with anhydrite (Fig. 6 d). Some of the calcite was interpreted to have formed during early diagenesis, based on the poikilotopic texture supporting the grain framework (Fig. 6 e), pre or syndating extensive mechanical compaction.

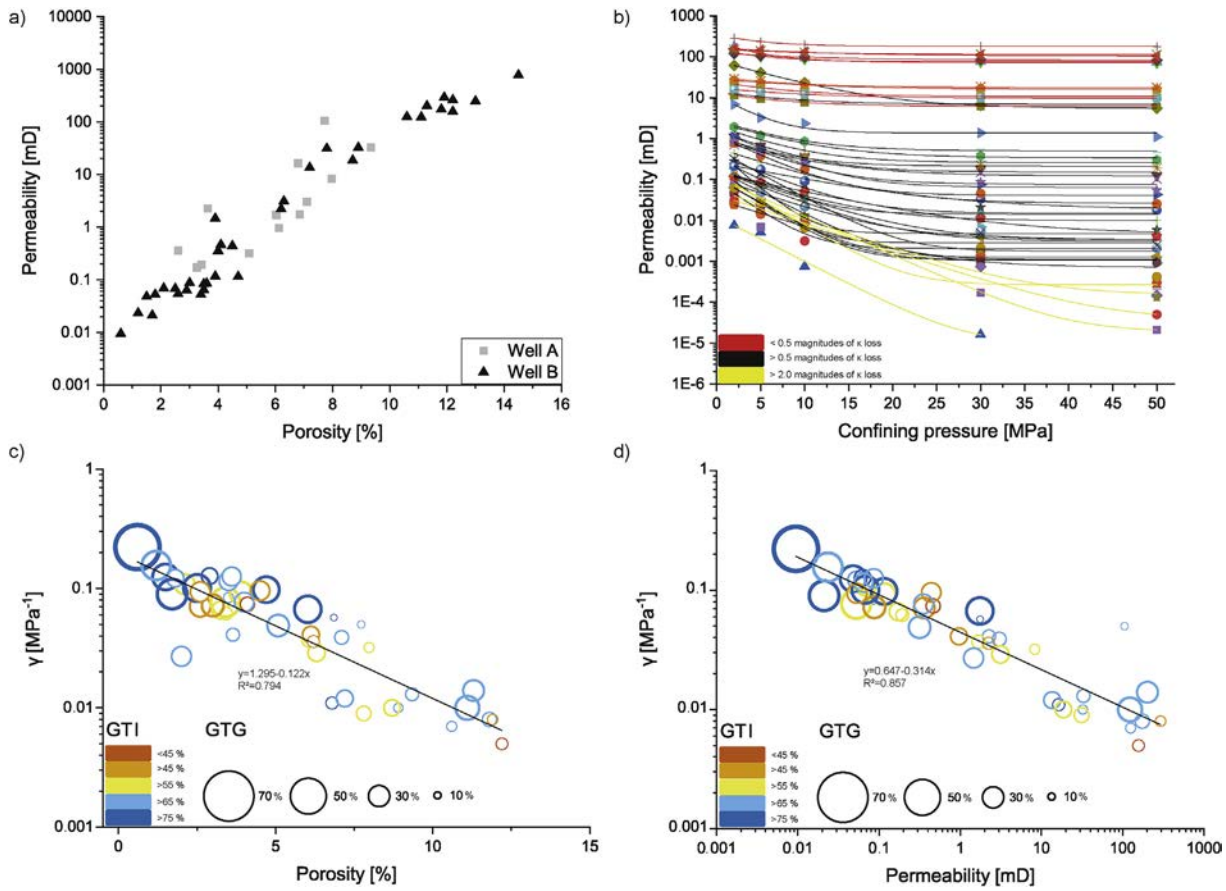

Fig. 9. a) Decane porosity compared to air permeability (1.2 MPa confining pressure), showing higher permeabilities in more porous horizons. b) He-permeability measured under decreasing confining pressures (50, 30, 10, 5 and 2 MPa) with exponential lines of best fit. c) Scatter plot of the pressure dependent permeability coefficient γ, determined after David et al. (1994), plotted versus decane porosity, with a linear line of best fit. d) Log-log scatter plot of γ versus air permeability (1.2 MPa confining pressure) with an exponential best fit.

5.1.2. Burial diagenesis

Due to textural relationships compared to authigenic quartz, ver micular chlorite was likely formed before the onset of quartz ce mentation, because vermicular chlorite was observed to grow in open pores and was observed to be encompassed by authigenic quartz (Fig. 6 g). The vermicular chlorite was often observed close to calcite cement (Fig. 6 b), which can be a byproduct of chloritization of kaolinite (Worden and Morad, 2003). However, this would require siderite as a precursor for the calcite phase, which was not observed. Either all siderite was consumed during the formation of chlorite, or it was never present. Alternatively, an external iron source via hydrothermal fluid circulation along the graben fault system could be interpreted to be the main source for reactants (Gaupp et al., 1993; Wüstefeld et al., 2017).

Based on textural observations (Fig. 5 b, Fig. 6 a b, g h, Fig. 7 a f), authigenic quartz is interpreted to be forming during burial diagenesis, requiring temperatures above 75 °C (Walderhau, 1994) respectively 80 °C (Worden and Morad, 2000) to be pervasive. Considering the modelled geothermal gradient of 37 °C/km (Schwarzer and Littke, 2007), the thermal conditions for quartz formation were reached in depths of approximately 2500 3000 m. Relative uplift during the Cre taceous (Fig. 10) possibly triggered by erosion due to the Late Albian transgression (Hancock and Kauffman, 1979), did not reduce the burial depth of the sedimentary Rotliegend below 2500 m (Schwarzer and Littke, 2007) (Fig. 10). According to Lander and Bonnell (2010), quartz cementation growth rates are significantly higher on non euhedral surfaces or fractures. Continuous clay mineral grain coatings can inhibit quartz cements from forming on quartz substrates (Heald and Larese, 1974; Storvoll et al., 2002; Ajdukiewicz et al., 2010; Busch et al., 2017, 2018). The correlation of quartz cement volumes in dependence of GTI coating coverages (Fig. 8c) supports this model and is interpreted to be a main control on the variability of authigenic quartz cement amounts in samples of this study. Authigenic quartz cement likely formed

Table 1
The six major empirical petrophysical and petrographic proxies and their observed values (minimum, maximum and arithmetic mean) used for determining the three rock types. Abbreviations: GTG = grain to grain illite coatings, GTI = grain to IGV illite coating, PF cmt = pore-filling cement.

	Type A	Type B	Type C
K	1.7–780.9 mD (Ø = 126 ± 40 mD)	0.053–3.13 mD (Ø = 0.59 ± 0.2 mD)	0.009–0.068 mD (Ø = 0.04 ± 0.01 mD)
Φ	6.8–14.5% (Ø = 9.8 ± 0.6%)	1.8–6.3% (Ø = 4.0 ± 0.3%)	0.6–2.5% (Ø = 1.8 ± 0.4%)
γ	0.005–0.057 MPa ^{1} (Ø = 0.019 ± 0.0033 MPa ^{1})	0.029–0.127 MPa ^{1} (Ø = 0.073 ± 0.0067 MPa ^{1})	0.077–0.220 MPa ^{1} (Ø = 0.129 ± 0.022 MPa ^{1})
GTG coating coverage	6.3–37.4% (Ø = 20.6 ± 1.7%)	10.1–44.1% (Ø = 27.3 ± 1.3%)	32.7–67.4% (Ø = 45.7 ± 4.7%)
GTI coating coverage	43.9.7–81.1% (Ø = 74.0 ± 1.4%)	40.7–85.2% (Ø = 62.1 ± 2.5%)	70.9–81.6% (Ø = 75.8 ± 3.3%)
PF cmt	3.7–14.0% (Ø = 8.6 ± 0.6%)	4.0–16.7% (Ø = 10.2 ± 0.7%)	2.7–11.3% (Ø = 7.5 ± 1.4%)

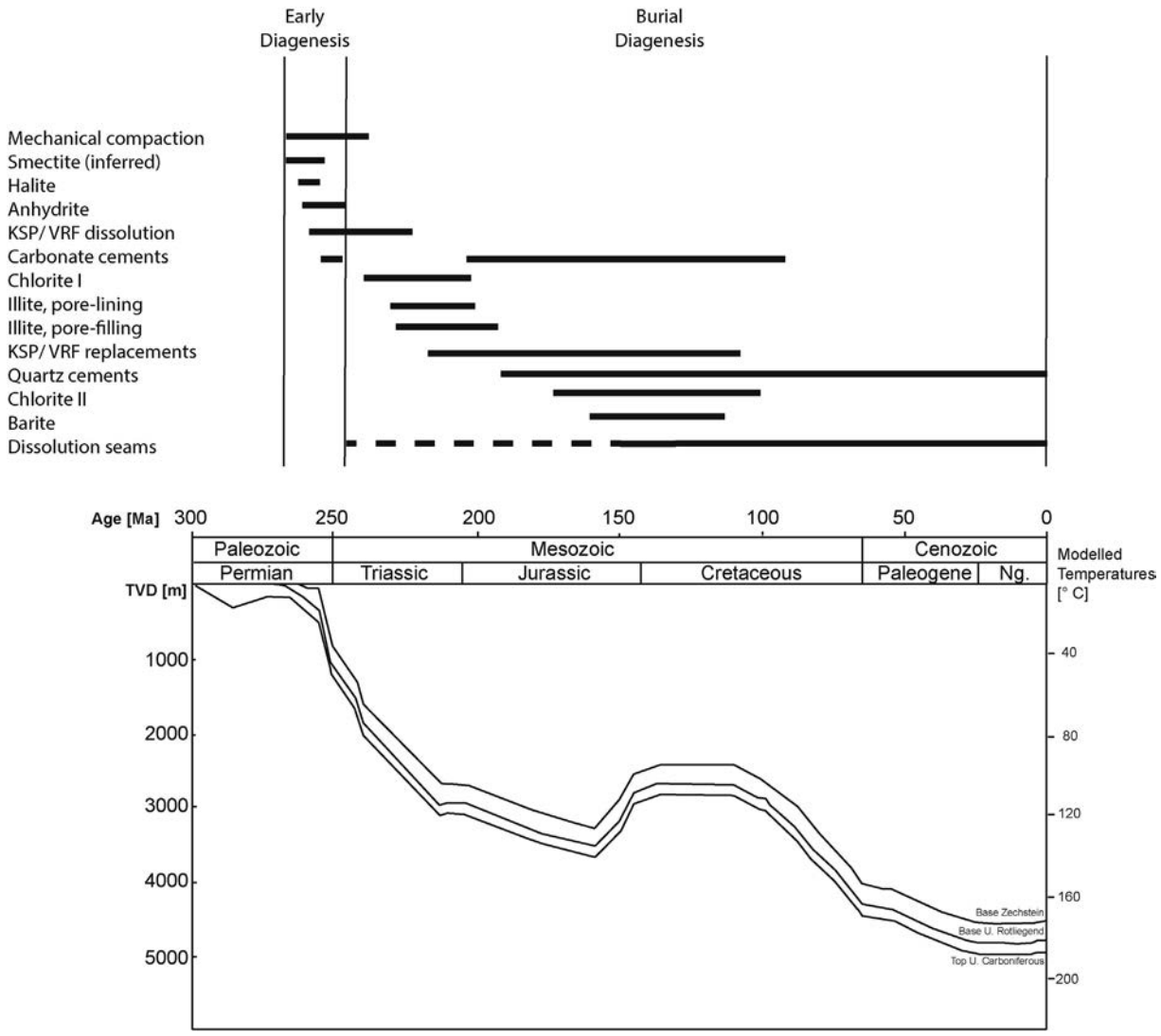

Fig. 10. Paragenetic sequence in correlation with the burial history for the most abundant cements and alterations. The paragenesis was reconstructed based on textural observations and cathodoluminescence. The burial history and the geothermal gradient (37 °C/km) were taken from Schwarzer and Littke (2007) and correlated to the paragenesis.

throughout the entire burial history since its initialization, as long as sufficient amounts of silica were available. Possible silica sources are autochthonous supply by the illitization of smectite (Worden and Morad, 2003) or from dissolution seams (Walderhaug and Bjørkum, 2003), as well as allochthonous hydrothermal fluids circulating through the Rotliegend strata (Gaupp et al., 1993).

Illite can recrystallize from smectite in the presence of a potassium source (Worden and Morad, 2003). It was differentiated between tangential pore lining illite and pore filling meshwork illite (Molenaar and Felder, 2018). Furthermore, illite replacements of potassium feldspars were observed, which likely formed during burial diagenesis (Worden and Morad, 2003). Meshwork illite in open pores was likely sourced by hydrothermal fluids, as there were no potassium feldspars observed in close proximity to them. Hydrothermal fluids are well documented in Rotliegend sandstones and have been interpreted to strongly influence mineral authigenesis during burial diagenesis (Sullivan et al., 1990; Gaupp et al., 1993; Zwingmann et al., 1998; Pudlo et al., 2012; Nadoll et al., 2019). Hydrothermal fluids were linked to the occurrence of fault systems in Rotliegend and Upper Carboniferous sandstones in the North German Basin (Gaupp et al., 1993). As the fault systems in the studied setting terminate in the overlying Zechstein evaporites (Gast and Gundlach, 2006), fluid flow from overlying stratigraphic units can be excluded due to the integrity of the salt seals (Gast et al., 2010). Consequentially, hot hydrothermal fluids, likely originating from underlying Carboniferous units, must have migrated along the graben faults of the Permo Carboniferous fault system (Gast and Gundlach, 2006). These fluids transported ions and heat into the system, which enabled the precipitation of late diagenetic alterations such as barite or late calcite (Gaupp et al., 1993; Zwingmann et al., 1999; Busch et al., 2019; Nadoll et al., 2019).

The second carbonate cement phase occurred in minor amounts in samples with intense authigenic quartz (Fig. 6 a), and in larger amounts in samples with low to none authigenic quartz (Fig. 6 b, h), but continuous tangential illite coatings. It was observed to overgrow both authigenic quartz (occasionally euhedral) (Fig. 6 g) and vermicular chlorite (Fig. 6 h). Small rims of authigenic quartz overgrown by calcite indicate that the cementation of late calcite began after the onset of quartz cementation, as the cementation of authigenic quartz is dependent on time exposed to sufficient temperatures and silica supply (Walderhau, 1994; Lander et al., 2008; Lander and Bonnell, 2010; Busch et al., 2018). As a result, the second calcite cement phase was likely formed after the onset of quartz cementation. The second calcite cement phase is interpreted to have formed after the vermicular chlorite based on textural observations, showing that calcite terminates

against vermicular chlorite (Fig. 6 b).

The pore occluding chlorite, which was heavily deformed and squeezed between the grains, showed no vermicular texture. It might have been either formed independently from the vermicular chlorite or lost its texture during mechanical and chemical compaction. As this chlorite only occurred in heavily compacted samples, while vermicular chlorite occurred in almost all other samples, the two species of chlorite are interpreted to be of the same origin. The structural differences are therefore just a consequence of the intense mechanical and chemical compaction and not an additional chlorite phase.

Authigenic barite occurs as pore filling cements enclosing euhedral syntaxial quartz cements (Fig. 6 c & Fig. 7 e f), implying the barite formed during the late burial diagenesis after authigenic quartz reached its euhedral shape (Busch et al., 2019).

Cathodoluminescence was used to assess the quartz cement content of samples containing serrated quartz grains (night blue luminescence) in samples with pervasive chemical compaction, as the interpretation of detrital and authigenic quartz was difficult due to the absence of grain coating phases (Fig. 6 a b). Authigenic quartz consistently did not show luminescence (Fig. 6 c d), as a result the consistently luminescent quartz in dissolution seams is interpreted to be of a detrital origin. Chemical compaction in return is discussed to be favored by the oc currence of grain coating illite around detrital quartz (Greene et al., 2009; Kristiansen et al., 2011). The maximum encountered IGV was 25.7%, which approximately matches the empirically determined maximum IGV of 26% purely by mechanical compaction (Paxton et al., 2002). However, observed IGVs as low as 11% cannot be attributed to mechanical compaction alone in an idealized sphere packing without major detrital ductile grains according to Paxton et al. (2002). While the studied sandstones contain some ductile detrital grains their content is not interpreted to be the main cause of low IGV samples. Including the sample's well sorting (moderately well to extremely well, supple mentary material) and their low detrital clay content (avg.: 0.9%, supplementary material), chemical compaction is interpreted to have reduced the IGV in these low IGV samples. Larger amounts of grain to grain illite grain coatings were observed to correlate with a decrease in the IGV (Fig. 7 c). Therefore, chemical compaction may be quantita tively assessed using the illite coverage on GTG interfaces compared to the IGV. As a result, illite coverage on GTG interfaces was interpreted to be the main controlling factor for the intensity of chemical compaction in different samples.

5.2. Reservoir quality assessment and rock typing

Rock typing attempts have been made to assess the reservoir quality and behavior under elevated pressure conditions. Based on petrophy sical and petrographic criteria, three types were distinguished (Fig. 11). These types were based on permeability, decane porosity, authigenic phases, clay mineral coatings, γ values, petrographic observations, detrital composition, and the reconstructed paragenetic sequence. Al though possibly relevant for the pressure sensitivity of permeability for individual samples, consistent trends for the influence of blocky ce ments, ductile rock fragments and sorting could not be established.

As permeability measurements under decreasing confining pres sures showed varying intensity in the permeability enhancement (Fig. 9 b), exponential lines of best fit analog to David et al. (1994) were used to quantify the exponential relationship between permeability and pressure sensitivity of permeability from 50 MPa to 2 MPa confining pressure. High decane porosity samples experienced permeability en hancement of less than one order of magnitude under decreasing con fining pressures, while low decane porosity samples were reduced by several orders of magnitude (Fig. 9 b). Similar observations have been made in a study on Rotliegend sandstones from a tight gas reservoir in northern Germany (Albrecht, 2015).

Due to the good empirical correlation between decane porosity and permeability (Fig. 9 a), between decane porosity and the pressure sensitivity of permeability (Fig. 9 c), as well as between permeability and the pressure sensitivity of permeability (Fig. 9 d), the petrophysical data allows a straight forward approach for reservoir quality assess ment and will be used synonymously for reservoir quality. The rock typing was conducted under consideration of the petrophysical data in combination with the main petrographic texture and resulting diage netic alteration attributed to the reduction or preservation of open porosity, thus linking certain diagenetic features and processes to pet rophysical properties (Fig. 11). As a result, three rock types were identified (Fig. 11). Type A shows intermediate to high decane poros ities (6.8% 14.5%, avg.: 9.8%) and permeabilities at 1.2 MPa confining pressure > 1 mD (1.7 780.9 mD, avg.: 126.7 mD) (Fig. 9 a). Perme ability was enhanced within the same order of magnitude under ele vated confining pressures from 50 to 2 MPa (Fig. 9 b), which is in agreement with observations in previous studies (David et al., 1994; Albrecht, 2015). Calculated γ values between 0.005 and 0.057 MPa^{-1} (Table 1, Fig. 11) are mostly in agreement with values for sandstones (0.0014 0.02 MPa^{-1}) stated by literature (Yale, 1984; David et al., 1994). Clay mineral grain coating coverages are mostly large (avg. GTI coverage: 74%, Table 1) on grain to IGV interfaces (Fig. 8 c, Fig. 11), which are known to inhibit quartz cement (avg.: 4.9%, Supplementary material) (Ajdukiewicz et al., 2010; Busch et al., 2017; Molenaar and Felder, 2018). Clay mineral coatings on grain to grain interfaces may occur (avg. GTG coverage: 21%), but they are not frequent enough to lead to intense chemical compaction. As a result, the pore space and pore throats of type A are relatively uncemented and open, represented by a moderate amount of intergranular cements (avg.: 8.6%). In sum mary, rock type A enabled to retain decane porosities > 6.5% as low to medium GTG coatings reduced the porosity loss by chemical compac tion, while medium to high GTI coatings minimized the amount of syntaxial quartz cements.

Type B is defined by intermediate to poor reservoir qualities with permeabilities at 1.2 MPa confining pressure generally below < 1 mD (0.053 3.13 mD, mean: 0.59 mD) and decane porosities < 6.5% (1.8 6.3%, mean: 4.0%). The permeability enhancement in type B ranges from 1 2 orders of magnitude, thus showing the similar per meability enhancements as Albrecht (2015) demonstrated for samples with comparable permeabilities. The γ values (avg.: 0.073 MPa^{-1}, Fig. 11) are in agreement with ranges for tight sandstones (> 0.038 MPa^{-1}) (Yale, 1984; David et al., 1994). Less continuous (avg. GTI coverage: 62%) illite coverages on grains in contact with the IGV were observed (Fig. 11, Table 1). Consequently, syntaxial quartz cement, occur in larger quantities than in type A (avg.: 10.2%, Fig. 11). This leads to a reduction in available open pore space and smaller pore throats, reducing porosity and permeability (Fig. 11). It needs to be considered that micro porosities in the pore filling chlorite/illite might have a positive effects on reservoir quality (Aagaard et al., 2000). Thus, the main process controlling the reduction in reservoir quality in type B are the low GTI coatings enabling intense syntaxial quartz cementation.

The pore volume of type C is almost completely occluded, resulting in low decane porosities (cutoff here: < 3%, 0.6 2.5%) and perme abilities at 1.2 MPa confining pressure (cutoff here: < 0.1 mD, 0.009 0.068 mD), and thus poor reservoir qualities (Fig. 11). Type C is characterized by permeability enhancements of > 2 orders of magni tude from 50 to 2 MPa confining pressure (Fig. 9 b, Fig. 11). γ values (avg.: 0.129 MPa^{-1}, Table 1) are the highest in this study, and do ex ceed values reported for tight sandstones (> 0.038 MPa^{-1}) (Yale, 1984; David et al., 1994).

The most extensive clay mineral coatings on GTG interfaces en countered in this study were observed in type C (33 67%, avg. GTG coverage: 46%, Fig. 11, Table 1). These intense GTG coatings are in terpreted to have enhanced chemical compaction (Greene et al., 2009; Kristiansen et al., 2011) due to the electrochemical potential difference between illite/muscovite and quartz (Kristiansen et al., 2011). Another characteristic are high amounts of illite coatings (avg. GTI coverage: 76%, Fig. 11, Table 1) on GTI interfaces as well as the lowest amount of

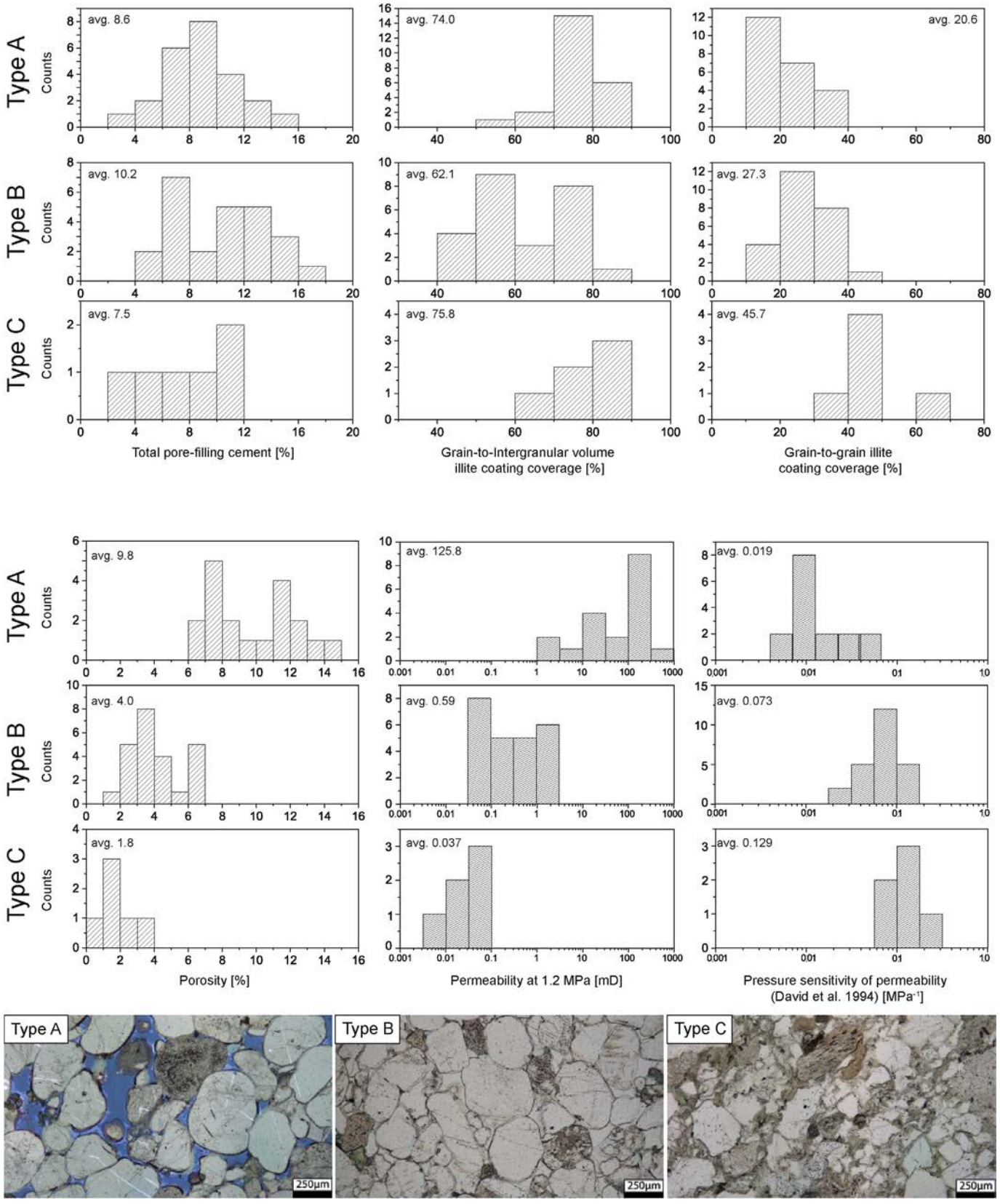

Fig. 11. Histograms of the statistical distribution of the petrographic (upper) and petrophysical (lower) data used to determine the rock type. Error bars and threshold values for these proxies are shown in Table 1. Typical examples of the textures of the three rock types are shown as photo-micrographs.

pore filling cements of the three rock types (avg.: 7.5%). Consequentially, reservoir quality in type C was primarily reduced by intense chemical compaction due to the high GTG coating coverages and the absence of pore filling syntaxial cements stabilizing the grain framework due to relatively large GTI grain coating coverages.

6. Conclusions

Reservoir quality in the studied wells is mainly controlled by compactional porosity loss due to mechanical compaction, syntaxial quartz overgrowth cements, and chemical compaction. Three rock types based on their different linked compactional and diagenetic alterations were defined based on the amount and location of illite coatings, as well as their decane porosity and their permeability under elevated confining pressures.

Type A is characterized by mostly continuous illite coatings (avg. GTI coverage: 74%) on grain to IGV (GTI) interfaces, which inhibited quartz cementation and preserved reservoir quality. Porosities (avg.: 9.8%) and permeabilities (avg.: 126 mD) are the highest among the studied rocks. The pressure sensitivity of permeability (avg.: 0.019 MPa^{-1}) is lowest, indicating a smaller reduction of permeability under elevated confining pressures.

Type B shows the most discontinuous illite coatings on GTI interfaces (avg. GTI coverage: 62%), as well as the highest amount of pore filling authigenic cements (avg.: 10.3%), especially quartz and calcite, occluded pore spaces and pore throats in Type B. As a result, decane porosity and permeability were reduced to an average of 4.0% and 0.59 mD. The pressure sensitivity (avg.: 0.073 MPa^{-1}) is larger than for type A.

Type C is characterized by the highest coverage of illite coatings on grain to grain (GTG) interfaces (avg. GTG coverage: 46%). In contrast to Type B, the illite coverages on GTI interfaces are high (avg. GTI coverage: 76%) while the amount of pore filling cements are the lowest (avg.: 7.5%). Intense chemical compaction was enabled due to the presence of illite coatings at the contacts of detrital quartz grains, thus reducing the IGV and preserved porosities (avg.: 1.8%). Consequently, permeability is also very low (avg.: 0.037 mD), and the pressure sensitivity of permeability is about a magnitude higher (avg.: 0.129 MPa^{-1}) compared to Type A and B.

The combination of petrophysical and petrographic data sets to form a coherent rock typing was shown to capture the variations in reservoir quality in these samples containing complex interactions of diagenetic and compaction processes.

Acknowledgements

We thankfully acknowledge the constructive comments by reviewers R. Fink and M. Kalifa and Associate Editor I. Al Aasm. We gratefully acknowledge research funding by the BMBF (Federal Ministry of Education and Research, research grant: FKZ 03A0007A) and sample provision by Wintershall DEA GmbH by H. M. Rumpel. D. Soyk (DGMK) is thanked for project coordination.

References

Aagaard, P., Jahren, J.S., Harstad, A.O., Nilsen, O., 2000. Formation of grain-coating chlorite in sandstones. Laboratory synthesized vs. natural occurrences. Clay Miner. 35, 261–269.

Ajdukiewicz, J.M., Larese, R.E., 2012. How clay grain coats inhibit quartz cement and preserve porosity in deeply buried sandstones: observations and experiments. AAPG (Am. Assoc. Pet. Geol.) Bull. 96, 2091–2119.

Ajdukiewicz, J.M., Nicholson, P.H., Esch, W.L., 2010. Prediction of deep reservoir quality using early diagenetic process models in the Jurassic Norphlet Formation, Gulf of Mexico. AAPG (Am. Assoc. Pet. Geol.) Bull. 94, 1189–1227.

Albrecht, D., 2015. Untersuchungen zum Spannungseinfluss auf die Fluiddurchlässigkeiten von Rotliegend Tight Gas Sandsteinen, Fakultät für Energie- und Wirtschaftswissenschaften. Technische Universität Clausthal, Clausthal-Zellerfeld, pp. 123.

Amann-Hildenbrand, A., Dietrichs, J.P., Krooss, B.M., 2015. Effective gas permeability of Tight Gas Sandstones as a function of capillary pressure – a non-steady-state approach. Geofluids 16, 367–383.

Ambrose, W.A., Lakshminarasimhan, S., Holtz, M.H., Núñez-López, V., Hovorka, S.D., Duncan, I., 2008. Geologic factors controlling CO2 storage capacity and permanence: case studies based on experience with heterogeneity in oil and gas reservoirs applied to CO2 storage. Environ. Geol. 54, 1619–1633.

Bachmann, G.H., Geluk, M.C., Warrington, G., Becker-Roman, A., Beutler, G., Hagdorn, H., Hounslow, M.W., Nitsch, E., Röhling, H.-G., Simon, T., Szulc, A., 2010. Triassic. In: Doornenbal, J.C., Stevenson, A.G. (Eds.), Petroleum Geological Atlas of the Southern Permian Basin Area. EAGE Publications, Houten, NL, pp. 149–173.

Bachu, S., 2000. Sequestration of CO2 in geological media: criteria and approach for site selection in response to climate change. Energy Convers. Manag. 41, 953–970.

Bahlis, A.B., De Ros, L.F., 2013. Origin and impact of authigenic chlorite in the Upper Cretaceous sandstone reservoirs of the Santos Basin, eastern Brazil. Pet. Geosci. 19, 185–199.

Becker, I., Busch, B., Koehrer, B., Adelmann, D., Hilgers, C., 2019. Reservoir quality evolution of Upper Carboniferous (Westphalian) tight gas sandstones, Lower Saxony Basin, NW Germany. J. Pet. Geol. 42, 371–392.

Becker, I., Wüstefeld, P., Koehrer, B., Felder, M., Hilgers, C., 2017. Porosity and permeability variations in a tight gas sandstone reservoir analogue, Westphalian D, Lower Saxony Basin, NW Germany: influence of depositional setting and diagenesis. J. Pet. Geol. 40, 363–390.

Binot, F., Gerling, P., Hiltmann, W., Kockel, F., Wehner, H., 1993. The petroleum system in the Lower Saxony Basin. In: Spencer, A.M. (Ed.), Generation, Accumulation and Production of Europe's Hydrocarbons. EAGE Special Publication, pp. 121–139.

Blakey, R.C., Wong, T.E., 2003. Carboniferous – Permian paleogeography of the assembly of Pangaea. In: Proceedings of the XVth International Congress on Carboniferous and Permian Stratigraphy, vol. 10. pp. 16.

Busch, B., Adelmann, D., Hilgers, C., 2020. Reservoir quality controls on Rotliegend fluvio-aeolian wells in Germany and The Netherlands, Southern Permian Basin – Impact of grain coatings and cements. Mar. Pet. Geol. 112.

Busch, B., Becker, I., Koehrer, K., Adelmann, D., Hilgers, C., 2019. Porosity evolution of two Upper Carboniferous tight-gas-fluvial sandstone reservoirs: impact of fractures and total cement volumes on reservoir quality. Mar. Pet. Geol. 100, 376–390.

Busch, B., Hilgers, C., Gronen, L., Adelmann, D., 2017. Cementation and structural diagenesis of fluvio-aeolian Rotliegend sandstones, northern England. J. Geol. Soc. 174, 855–868.

Busch, B., Hilgers, C., Lander, R.H., Bonnell, L.M., Adelmann, D., 2018. Reservoir quality and burial model evaluation by kinetic quartz and illite cementation modeling: case study of Rotliegendes, north Germany. AAPG (Am. Assoc. Pet. Geol.) Bull. 102, 293–307.

Busch, B., Winkler, R., Osivandi, K., Nover, G., Amann-Hildenbrand, A., Hilgers, C., 2015. Evolution of small-scale flow barriers in German Rotliegend siliciclastics. Geol. Soc. Spec. Publ. 435, 141–160.

Chandler, M.A., Kocurek, G., Goggin, D.J., Lake, L.W., 1989. Effects of stratigraphic heterogeneity on permeability in eolian sandstone sequence, Page Sandstone, northern Arizona. AAPG (Am. Assoc. Pet. Geol.) Bull. 73, 658–668.

David, C., Wong, T.-F., Zhu, W., Zhang, J., 1994. Laboratory measurement of compaction-induced permeability change in porous rocks: implications for the generation and maintenance of pore pressure excess in the crust. Pure Appl. Geophys. 143, 425–456.

Desbois, G., Urai, J.L., Hemes, S., Schröppel, B., Schwarz, J.-O., Mac, M., Weiel, D., 2016. Multi-scale analysis of porosity in diagenetically altered reservoir sandstone from the Permian Rotliegend (Germany). J. Pet. Sci. Eng. 140, 128–148.

Esch, W.L., Ajdukiewicz, J.M., Reynolds, A.C., 2008. Early Grain-Coat Formation in Chaco Dune Field , New Mexico : Insight into Formation Mechanisms , Distribution , and Implications for Predictive Modeling to Assist in Deep Play Identification. AAPG Annual Convention, San Antonio, Texas.

Folk, R.L., 1980. Petrology of the Sedimentary Rocks. Hemphill Pub. Co, Austin, Texas.

Fryberger, S.G., Knight, R., Hern, C., Moscariello, A., Kabel, S., 2011. Rotliegend facies, sedimentary provinces, and stratigraphy, Southern Permian Basin UK and The Netherlands: a review with new observations. In: Grötsch, J., Gaupp, R. (Eds.), The Permian Rotliegend of The Netherlands. SEPM Special Publication.

Gast, R., Gundlach, T., 2006. Permian strike slip and extensional tectonics in Lower Saxony , Germany. Z. dt. Ges. Geowiss. 157, 41–56.

Gast, R.E., 1993. Sequenzanalyse von äolischen Abfolgen im Rotliegenden und deren Verzahnung mit Küstensedimenten. Geol. Jahrb. 131, 117–139.

Gast, R.E., Dusar, M., Breitkreuz, C., Gaupp, R., Schneider, J.W., Stemmerik, L., Geluk, M.C., Geißler, M., Kiersnowski, H., Glennie, K.W., Kabel, S., Jones, N.S., 2010. Rotliegend. In: Doornenbaal, H., Stevenson, A. (Eds.), Petroleum Geological Atlas of the Southern Permian Basin Area. EAGE, Houten, pp. 101–121.

Gaupp, R., Matter, A., Platt, J., Ramseyer, K., Walzebuck, J., 1993. Diagenesis and fluid evolution of deeply buried Permian (Rotliegende) gas reservoirs, northwest Germany. AAPG (Am. Assoc. Pet. Geol.) Bull. 77.

Gaupp, R.O., Jos, A., 2011. Diagenesis and Reservoir Quality of Rotliegend Sandstones in the Nortern Netherlands - A Review 98 SEPM Special Publication.

Geluk, M.C., 1999. Late Permian (Zechstein) rifting in The Netherlands: models and implications for petroleum geology. Pet. Geosci. 5, 189–199.

Geluk, M.C., 2005. Stratigraphy and Tectonics of Permo-Triassic Basins in the Netherlands. Utrecht University.

Glennie, K.W., 2007. The Permo-carboniferous Rotliegend of NW Europe. In: Proceedings of the XVth International Congress on Carboniferous and Permian Stratigraphy. Netherlands Academy of Arts and Sciences, Amsterdam, pp. 10–16.

Glennie, K.W., Buller, A.T., 1983. The Permian Weissliegend of NW Europe: the partial

deformation of aeolian dune sands caused by the Zechstein transgression. Sediment. Geol. 35, 43–81.
Greene, G.W., Kristiansen, K., Meyer, E.E., Boles, J.R., Israelachvili, J.N., 2009. Role of electrochemical reactions in pressure solution. Geochem. Cosmochim. Acta 73, 2862–2874.
Hancock, J.M., Kauffman, E.G., 1979. The great trangsressions of the Late Cretaceous. J. Geol. Soc. 136, 175–186.
Heald, M.T., Larese, R.E., 1974. Influence of coatings on quartz cementation. J. Sediment. Petrol. 44, 1269–1274.
Hoth, K., Huebscher, H.D., Korich, D., Gabriel, W., Enderlein, F., 1993. Die Lithostratigraphie der permokarbonischen Effusiva im Zentralabschnitt der mitteleuropäischen Senke. Geol. J. A 131, 179–196.
Houseknecht, D.W., 1987. Assessing the relative importance of compaction processes and cementation to reduction of porosity in sandstones. AAPG (Am. Assoc. Pet. Geol.) Bull. 71, 633–642.
Katzung, G., 1988. Tectonics and sedimentation of variscan molasses in central-Europe. Z. Geol. Wiss. 16, 823–843.
Kiersnowski, H., 2013. Depositional development of the Polish Upper Rotliegend Basin and evolution of its sediment source areas. Geol. Q. 41, 433–455.
Kiersnowski, H., Paul, J., Peryt, T.M., Smith, D.B., 1995. Facies, Paleogeography, and Sedimentary History of the Southern Permian Basin in Europe, the Permian of Northern Pangea. Springer, Berlin 199-136.
Kley, J., Voigt, T., 2008. Late Cretaceous intraplate thrusting in central Europe: effect of Africa-Iberia-Europe convergence, not Alpine collision. Geology 36, 839–842.
Klinkenberg, L.J., 1941. The Permeability of Porous Media to Liquids and gases., Drilling and Production Practice. American Petroleum Institute.
Knox, R.W.O.B., Bosch, J.H.A., Rasmussen, E.S., Heilmann-Clausen, C., Hiss, M., De Lugt, I.R., Kasińksi, J., King, C., Köthe, A., Słodkowska, B., Standke, G., Vandenberghe, N., 2010. Cenozoic. In: Doornenbal, J.C., Stevenson, A.G. (Eds.), Petroleum Geological Atlas of the Southern Permian Basin Area. EAGE Publication b.v., Houten, pp. 211–223.
Kocurek, G., Robinson, N.I., Sharp Jr., J.M., 2001. The response of the water table in coastal aeolian systems tochanges in sea level. Sediment. Geol. 139, 1–13.
Kristiansen, K., Valtiner, M., Greene, G.W., Boles, J.R., Israelachvili, J.N., 2011. Pressure solution – the importance of the electrochemical surface potentials. Geochem. Cosmochim. Acta 75, 6882–6892.
Kuila, U., McCarthy, D.K., Derkowski, A., Fisher, T.B., Prasad, M., 2014. Total porosity measurement in gas shales by the water immersion porosimetry (WIP) method. Fuel 117, 1115–1129.
Lander, R.H., Bonnell, L.M., 2010. A model for fibrous illite nucleation and growth in sandstones. AAPG (Am. Assoc. Pet. Geol.) Bull. 94, 1161–1187.
Lander, R.H., Larese, R.E., Bonnell, L.M., 2008. Toward more accurate quartz cement models: the importance of euhedral versus noneuhedral growth rates. AAPG (Am. Assoc. Pet. Geol.) Bull. 92, 1537–1563.
Legarth, B., Huenges, E., Zimmermann, G., 2005. Hydraulic fracturing in a sedimentary geothermal reservoir: Results and implications. Int. J. Rock Mech. Min. Sci. 42, 1028–1041.
Legler, B.S., Jörg, W., 2008. Marine ingressions into the Middle/Late Permian saline lake of the Southern Permian Basin (Rotliegend, Northern Germany) possibly linked to sea-level highstands in the Arctic rift system. Palaeogeogr. Palaeoclimatol. Palaeoecol. 267, 102–114.
Liewig, N., Clauer, N., 2000. K-Ar dating of varied microtextural illite in Permian gas reservoirs, northern Germany. Clay Miner. 35, 271–281.
Line, H.L., Jahren, J., Hellevang, H., 2018. Mechanical compaction in chlorite-coated sandstone reservoirs – Examples from Middle – Late Triassic channels in the southwestern Barents Sea. Mar. Pet. Geol. 96, 348–370.
Lohr, T., Kramczyk, C.M., Tanner, D.C., Samiee, R., Endres, H., Oncken, O., Trappe, H., Kukla, P.A., 2007. Strain partitioning due to salt: insights from interpretation of a 3D seismic data set in the NW German Basin. Basin Res. 19, 579–597.
Lott, G.K., Wong, T.E., Dusar, M., Andsbjerg, J., Mönnig, E., Feldman-Olszewska, A., Verreussel, R.M.C.H., 2010. Jurassic. In: Doornenbal, J.C., Stevenson, A.G. (Eds.), Petroleum Geological Atlas of the Southern Permian Basin Area. EAGE Publications, Houten, NL, pp. 175–193.
Lundegard, P.D., 1992. Sandstone porosity loss - a "big Picture" view of the importance of compaction. J. Sediment. Petrol. 62, 250–260.
McCann, T., 1998. Sedimentary geology sandstone composition and provenance of the Rotliegend of the NE German basin. Sediment. Geol. 116, 177–198.
Menning, M., 1995. A numerical time scale for the Permian and Triassic periods: an integrated time analysis. In: Scholle, P.A., Peryt, T.M., Ulmer-Scholle, D.S. (Eds.), The Permian of Northern Pangea. Springer, Berlin, Heidleberg.
Moeck, I., Schandelmeier, H., Holl, H.G., 2009. The stress regime in a Rotliegend reservoir of the Northeast German Basin. Int. J. Earth Sci. 98, 1643–1654.
Molenaar, N., Felder, M., 2018. Clay cutans and the origin of illite rim cement: an example from the siliciclastic Rotliegend sandstone in the Dutch southern Permian Basin. J. Sediment. Res. 88, 641–658.
Morad, S., Al-Ramadan, K., Ketzer, J.M., De Ros, L.F., 2010. The impact of diagenesis on the heterogeneity of sandstone reservoirs: A review of the role of depositional fades and sequence stratigraphy. AAPG (Am. Assoc. Pet. Geol.) Bull. 94, 1267–1309.
Nadoll, P., Sośnicka, M., Kraemer, D., Duschl, F., 2019. Post-Variscan structurally-controlled hydrothermal Zn-Fe-Pb sulfide and F-Ba mineralization in deep-seated Paleozoic units of the North German Basin: a review. Ore Geol. Rev. 106, 273–299.
Paxton, S.T., Szabo, J.O., Ajdukiewicz, J.M., Klimentidis, R.E., 2002. Construction of an intergranular volume compaction curve for evaluating and predicting compaction and porosity loss in rigid-grain sandstone reservoirs. AAPG (Am. Assoc. Pet. Geol.) Bull. 86, 2047–2067.
Plein, E., van Adrichem Boogaert, A., 1995. Stratigraphie von Deutschland. Band 1. Norddeutsches Rotliegendbecken. Teil 2. Rotliegend-Monographie. Courier Forschungsinstitut Senckenberg 183, 1–193.
Pudlo, D., Reitenbach, V., Albrecht, D., Ganzer, L., Gernert, U., Wienand, J., Kohlhepp, B., Gaupp, R., 2012. The impact of diagenetic fluid–rock reactions on Rotliegend sandstone composition and petrophysical properties (Altmark area, central Germany). Environ Earth Sci 67, 369–384.
Rieke, H., 2001. Sedimentologie, Faziesarchitektur und Faziesentwicklung des kontinentalen Rotliegenden im Norddeutschen Becken (NEDB). GFZ, Potsdam, Germany.
Schmidt, C., Busch, B., Hilgers, C., 2018. Coupling Diagenesis and Petrophysics in Red Bed Siliciclastics to Infer Fluid Flow Anisotropies – Analog Studies from SW Germany. EAGE Annual. EAGE, Copenhagen.
Schöner, R., 2006. Comparison of Rotliegend Sandstone Diagenesis from the Northern and Southern Margin of the North German Basin, and Implications for the Importance of Organic Maturation and Migration. University of Jena.
Schröder, L., Plein, E., Bachmann, G.-H., Gast, R.E., Gebhardt, U., Graf, R., Helmuth, H.-J., Pasternak, M., Porth, H., Süssmuth, S., 1995. Stratigraphische Neugliederung des Rotliegend im Norddeutschen Becken. Geol. Jahrb. 148, 3–21.
Schwarzer, D., Littke, R., 2007. Petroleum generation and migration in the 'Tight Gas' area of the German Rotliegend natural gas play: a basin modelling study. Pet. Geosci. 13, 37–62.
Scotese, C.R., Langford, R.P., 1995. Pangea and the Paleogeography of the Permian. The Permian of Northern Pangea. Springer, Berlin, pp. 3–19.
Selley, R.C., 1998. Elements of Petroleum Geology. Gulf Professional Publishing.
Smith, D.B., 1979. Rapid marine transgressions and regressions of the Upper Permian Zechstein Sea. J. Geol. Soc. 136, 155–156.
Storvoll, V., Bjørlykke, K., Karlsen, D., Saigal, G., 2002. Porosity preservation in reservoir sandstones due to grain-coating illite: a study of the Jurassic Garn Formation from the Kristin and Lavrans fields, offshore Mid-Norway. Mar. Pet. Geol. 19, 767–781.
Sullivan, M.D., Haszeldine, R.S., Fallick, A.E., 1990. Linear coupling of carbon and strontium isotopes in Rotliegend Sandstone, North Sea: Evidence for cross-formational fluid flow. Geology 18, 1215–1218.
Sweet, M.L., 1999. Interaction between aeolian, fluvial and playa environments in the Permian Upper Rotliegend group, UK southern North Sea. Sedimentology 46, 171–187.
Taylor, T.R., Giles, M.R., Hathon, L.A., Diggs, T.N., Braunsdorf, N.R., Birbiglia, G.V., Kittridge, M.G., MacAulay, C.I., Espejo, I.S., 2010. Sandstone diagenesis and reservoir quality prediction: models, myths, and reality. AAPG (Am. Assoc. Pet. Geol.) Bull. 94, 1093–1132.
Taylor, T.R., Kittridge, M.G., Winefield, P., Bryndzia, L.T., Bonnell, L.M., 2015. Reservoir quality and rock properties modeling - Triassic and Jurassic sandstones, greater Shearwater area, UK Central North Sea. Mar. Pet. Geol. 65, 1–21.
Vejbæk, O.V., Andersen, C., Dusar, M., Herngreen, G.F.W., Krabbe, H., Leszczyński, K., Lott, G.K., Mutterlose, J., Van der Molen, A.S., 2010. Cretaceous. In: Doornenbal, J.C., Stevenson, A.G. (Eds.), Petroleum Geological Atlas of the Southern Permian Basin Area. EAGE Publications b.v., Houten, pp. 195–209.
Walderhau, O., 1994. Temperatures of quartz cementation in Jurassic sandstones from the Norwegian Continental Shelf - Evidence from fluid inclusions. J. Sediment. Res. 64, 311–323.
Walderhaug, O., Bjørkum, P.A., 2003. The effect of stylolite spacing on quartz cementation in the Lower Jurassic Stø Formation, southern Barents Sea. J. Sediment. Res. 73, 146–156.
Worden, R.H., Armitage, P.J., Butcher, A., Churchill, J., Csoma, A., Hollis, C., Lander, R., Omma, J., 2018. Petroleum reservoir quality prediction : overview and contrasting approaches from sandstone and carbonate communities. In: Armitage, P.J., Butcher, A.R., Churchill, J.M., Csoma, A.E., Hollis, C., Lander, R.H., Omma, J.E., Worden, R.H. (Eds.), Reservoir Quality of Clastic and Carbonate Rocks: Analysis, Modelling and Prediction. Geological Society of London.
Worden, R.H., Burkley, S.D., 2003. Sandstone diagenesis: the evolution of sand to stone. In: Burley, S.D., Worden, R.H. (Eds.), Sandstone Diagenesis: Recent and Ancient. Wiley Blackwell, pp. 2–44.
Worden, R.H., Morad, S., 2000. Quartz cementation in oil field sandstones: a review of the key controversies. Quartz Cementation in Sandstones 1–20.
Worden, R.H., Morad, S., 2003. Clay minerals in sandstones: controls on formation, distribution and evolution. Clay Mineral Cements in Sandstones 1–41.
Wüstefeld, P., Hilse, U., Koehrer, B., Adelmann, D., Hilgers, C., 2017a. Critical evaluation of an Upper Carboniferous tight gas sandstone reservoir analog: diagenesis and petrophysical aspects. Mar. Pet. Geol. 86, 689–710.
Wüstefeld, P., Hilse, U., Lüders, V., Wemmer, K., Koehrer, B., Hilgers, C., 2017. Kilometer-scale fault-related thermal anomalies in tight gas sandstones. Mar. Pet. Geol. 86, 288–303.
Yale, D.P., 1984. Network Modelling of Flow, Storage and Deformation in Porous Rocks. Department of Geophysics. Stanford University, Stanford.
Ziegler, P.A., 1990. Geological Atlas of Western and Central Europe.
Ziegler, P.A., Dezes, P., 2005. Crustal evolution of western and central Europe. In: Gee, D., Stephenson, R.A. (Eds.), Europe Lithosphere Dynamics. Geological Society, London.
Zwingmann, H., Clauer, N., Gaupp, R., 1998. Timing of fluid flow in a sandstone reservoir of the north German Rotliegend (Permian) by K-Ar dating of related hydrothermal illite. In: Parnell, J. (Ed.), Dating and Duration of Fluid Flow and Fluid-Rock Interaction. Geological Society, London, pp. 91–106.
Zwingmann, H., Clauer, N., Gaupp, R., 1999. Structure-related geochemical (REE) and isotopic (K-Ar, Rb-Sr, d18O) characteristics of clay minerals from Rotliegend sandstone reservoirs (Permian, northern Germany). Geochem. Cosmochim. Acta 63, 2805–2823.